



Full length article



Phase transitions in alumina films during post-sparking anodising of Al alloys

Etienne Bousser^{a,b,*}, Aleksey Rogov^{a,c}, Pavel Shashkov^d, Ali Gholinia^a, Nicolas Laugel^{a,c}, Thomas J.A. Slater^e, Philip J. Withers^{a,c}, Allan Matthews^{a,c}, Aleksey Yerokhin^{a,c,*}

^a The University of Manchester, Department of Materials, Manchester, United Kingdom

^b Polytechnique Montréal, Center for Characterization and Microscopy of Materials, (CM)², Montreal, Canada

^c Henry Royce Institute, The University of Manchester, Manchester, United Kingdom

^d Cambridge Nanolitic Ltd., Haverhill, Suffolk, United Kingdom

^e Cardiff Catalysis Institute, School of Chemistry, Cardiff University, Cardiff, United Kingdom

ARTICLE INFO

Keywords:

Alpha alumina
Phase transition
EBSD
Grain size
Plasma Electrolytic Oxidation
Post-sparking anodising
Al alloy

ABSTRACT

Formation of the high-temperature α -Al₂O₃ phase during Plasma Electrolytic Oxidation of aluminium at ambient bulk temperatures has been previously attributed to local microdischarge events providing multiple melting-solidification cycles in micro-volumes of the surface oxide layer. In this work, it is demonstrated that the α phase can be formed even if the microdischarge is fully suppressed under specific processing conditions. Oxide layers produced in the post-sparking anodising mode were studied by FIB, TEM, EBSD, EDS and GDOES techniques to reveal microstructural and chemical evolutions that accompany the γ to α alumina transition. Our results provide strong evidence that the α phase can form spontaneously in regions of oxide with the appropriate temperature, grain size and impurity distributions in the γ -Al₂O₃ matrix that allow sufficient mobility of α/γ grain boundaries. Ionic migration within the oxide and hydrothermal dissolution/precipitation in the associated microporous network that facilitate species mobility at the grain boundaries allow the critical temperature for activation of $\gamma \rightarrow \alpha$ transition to be reduced. Overall, it is suggested that oxide layer growth can be considered in terms of a relatively simple Plug Flow Reactor model. This can help predict the phase transition kinetics depending on key processing parameters such as current density and frequency of pulse polarisation, thus enabling optimum control of coating microstructure for specific application requirements.

1. Introduction

Aluminium is one of the most ubiquitous engineering materials due to its protective oxide scale which forms naturally on the surface of this chemically active metal. Despite the wide range of coatings and surface engineering strategies that have been developed in recent decades, augmentation of this scale, e.g. by anodic polarisation in appropriate electrolytes, remains the most common way of protecting Al alloys from the harsh conditions and demanding environments inherent to the aerospace and transport industries [1]. Anodising of Al has been used industrially for nearly a century to grow relatively thick and conformal surface oxide films with very good adhesion [2]. However, amorphous alumina formed by anodising cannot provide adequate barrier protection from wear and corrosion without additional post-treatments.

Enhancement of the wear resistance of anodic alumina requires the

formation of hard crystalline phases, which is difficult to achieve *in situ* by conventional anodising. Crystallisation of amorphous Al₂O₃ can be triggered by heating, or application of ion- or electron-beams and other energetic impacts, as well as sufficiently high electric fields [3]. While many metastable alumina polymorphs exist, e.g. defect spinel structured γ phase, it is often the thermodynamically stable trigonal α -Al₂O₃ phase (i.e. corundum) that is desired due to its high mechanical and dielectric properties, as well as thermal and chemical stability [4]. Thermally induced formation of the α -Al₂O₃ phase normally requires elevated temperatures in the region 800 to 1200 °C which is inappropriate for Al due to its lower melting temperature. However, *in situ* crystallisation of the growing anodic alumina may be triggered at moderately elevated bulk substrate temperatures (100 to 250 °C), for example by anodising in molten salt baths [5], or by high instantaneous surface temperatures caused by local dielectric breakdown of the surface oxide layer [6]. The

* Corresponding authors.

E-mail addresses: etienne.bousser@polymtl.ca (E. Bousser), aleksey.yerokhin@manchester.ac.uk (A. Yerokhin).

<https://doi.org/10.1016/j.actamat.2022.118587>

Received 11 August 2022; Received in revised form 5 November 2022; Accepted 3 December 2022

Available online 4 December 2022

1359-6454/© 2022 The Author(s). Published by Elsevier Ltd on behalf of Acta Materialia Inc. This is an open access article under the CC BY license (<http://creativecommons.org/licenses/by/4.0/>).

latter approach is utilised in Plasma Electrolytic Oxidation (PEO) – an electrochemical technique for the deposition of relatively thick oxide ceramic coatings on so-called valve metals (Mg, Al, Ti, Zr, Nb, Ta, W etc.) [7–9]. PEO treatments are carried out under high anodic bias (typically up to 800 V) which induces local dielectric breakdown of the growing anodic oxide film. The resulting plasma microdischarges affect surface morphology, chemical and phase composition, yielding ceramic coatings with high adhesion (typical of anodically formed oxides), superior protective and functional properties attributed to crystalline α - and γ -Al₂O₃ phases.

It is known that the content of alpha alumina can be increased in dense PEO coatings formed on Al by using alternating current polarisation instead of DC [10]. Such current modes are characterised by a ratio of average negative to positive current densities, $R = j_{\text{Neg}} / j_{\text{Pos}}$. A particularly noticeable refinement in coating morphology can be achieved using a so-called ‘soft sparking’ PEO mode, where $R > 1$ [11–13]. The soft sparking is manifested as a weakening of apparent microdischarge activity, which occurs following an induction period wherein the oxide layer grows to a certain thickness in a conventional PEO mode, usually at a constant current density [10,14]. Surprisingly, discharge suppression often facilitates both coating growth and the formation of the crystalline α -Al₂O₃ phase [13,15]. This contradicts common understanding that the former process relies upon an ejection of Al into the electrolyte via discharge channels and the latter upon extremely high temperatures developed within a microdischarge. Until now, few attempts have been undertaken to account for the effects of cathodic current on the $\gamma \rightarrow \alpha$ phase transformation in PEO alumina, with explanations based on various sources of heat, e.g. from cathodic discharges [16–18], powerful anodic discharges [19,20] or intense exothermic oxidation of Al substrate [21], being proposed. These speculative conjectures need to be critically reassessed since the common underlying hypothesis based on the heat dissipated in plasma microdischarges affecting the surrounding material [22], i.e. causing its melting, evaporation and gas-phase redox reactions at the heating stage, followed by product sintering and quenching upon cooling from above 1000 °C – which is thought to enable the formation of α -Al₂O₃ – becomes inconsistent with the observed increases in the alpha phase content when the microdischarge is significantly weakened, or even completely suppressed [13]. In fact, the role of cathodic microdischarges has already been disproved by synchronous monitoring of light emission and current pulses together with consequent phase analysis demonstrating that α -Al₂O₃ appears much earlier than any cathodic discharges could be detected, which occurs only at the final stage of the process to the detriment of the coating microstructure [23,24].

Since the current ratio, R , plays a key role in the transition to soft sparking, galvanostatic control over the PEO process may seem to be preferable to potentiostatic or power control modes. However, the onset of soft sparking under constant current conditions can be delayed significantly (for up to 40...60 min, depending on j_{Pos} and R values) [13, 25,26], hampering the morphological refinement in already formed oxide. Here, we have attempted to overcome this issue by growing the oxide layer in a potentiostatic mode. This establishes non-stationary conditions with initially high j_{Pos} and R values that gradually decrease as the layer grows, which facilitates a transition to soft sparking and, in some cases, leads to complete elimination of discharge. Importantly, this is expected to promote both early morphological refinement and formation of the desired α alumina in relatively thin PEO coatings, making them more economically competitive with, and functionally superior to, conventional anodic oxide films. Furthermore, we have endeavoured to address the most intriguing fundamental question: how does the α phase form in PEO alumina in the absence of apparent plasma discharge? For this purpose, we used a combination of advanced micro (SEM, EDS, EBSD, TKD, TEM and FIB preparation) and macroscopic analytical techniques (XRD and GDOES) to study the oxide layer microstructure and alloying impurities distribution in conjunction with field effects imposed by bipolar polarisation. The insights provided by this study are

anticipated to contribute to both better understanding of the fundamental materials science of anodic alumina and the development of the next generation of anodising processes.

2. Experimental

2.1. Coating preparation

2.1.1. Materials

Commercial 6082 aluminium alloy plate (typical composition in wt. %: Si 0.7-1.3, Mg 0.6-1.2, Mn 0.4-1.0, Fe < 0.5, Cr < 0.25, Zn < 0.2, Cu < 0.1, Ti < 0.1, other < 0.15, Al balance) was cut into samples, 6 mm × 8 mm × 17 mm in size and degreased with acetone before processing. The aqueous electrolyte containing (mM): 22.3 KOH and 1.1 Na₄P₂O₇·10H₂O (both CP grade, Alfa Aesar; pH = 12.5; κ = 6.5 mS/cm) was kept in the temperature range 20 to 35 °C.

2.1.2. PEO treatment

The samples were processed using a pulsed bipolar (PB) PEO mode under potentiostatic control. Three levels of positive (470, 500, 530 V) and negative (220, 240, 255 V) voltage were used in the 3²-factorial experiment. The polarisation was provided by two MDX II DC voltage sources (30 and 15 kW, Advanced Energy) connected to the cell via a SPIK-2000A pulsing unit (MELEC GmbH) with a working frequency $f = 2.63$ kHz ($T_{\text{on}} = T_{\text{off}} = 180$ μ s, $T_{\text{on}}^+ = T_{\text{off}}^- = 10$ μ s). Each process started with a 30 s voltage ramp from zero to the pre-set level.

The transition to the soft sparking in the case of varying current values was determined by Optical Emission Spectrometry (OES) by a decrease in atomic line intensity. Atomic spectral lines of H (656.3 nm), Al (390.1 nm), Na (589.0 nm) and K (766.5 nm) identified according to the NIST database [27] were monitored using a Flotron fibre optic spectrometer (Nova Fabrica) with a 2 s exposure time.

2.2. Materials characterisation

2.2.1. Surface roughness

Surface roughness was evaluated using a Keyence X200K 3D Laser Microscope. The roughness parameter values were calculated using the average of 20 line profiles (~90 μ m length) uniformly distributed over the scanned area of 135 μ m × 95 μ m.

2.2.2. Cross-section preparation

Coating cross-sections were prepared in two ways. For general imaging and porosity evaluation, the formed oxide layers were sputter-coated with a chromium protective layer, mounted in a phenolic compound and ground using SiC papers down to p4000 grit size. Then the cross-sections were finely polished in an FEI Helios dual-beam Xe⁺ ion Plasma Focused Ion Beam (P-FIB) system using a rock-milling approach [28]. From these cross-sections, lamellas were prepared for subsequent TEM and Transmission Kikuchi Diffraction (TKD) measurements [29] (see Fig.S1 in Supplementary Materials available in the on-line version of this article).

For large area Electron Back Scattered Diffraction (EBSD) measurements, cross-sections were prepared by Ar⁺ Broad Ion Beam (BIB) milling with a Gatan Iliion II system using energies from 6 keV down to 0.5 keV. This approach minimised surface amorphisation and unexpected phase changes induced by ion milling enabling accurate identification of γ -Al₂O₃ grains.

2.2.3. Phase analysis

Identification of coating phase composition was performed by X-ray Diffraction (XRD) with a D8 Discovery diffractometer using Cu_{K α} radiation. Phase localisation, grain size distribution, orientation and coating texture were evaluated by EBSD and TKD using an FEI Magellan 400 XHR FEG-SEM equipped with a NordlysNano EBSD detector. The data were analysed using Oxford Instruments HKL Channel 5 software

employing the following structure parameters for the phases identified: Al (cubic, $m\bar{3}m$, $a = 4.05\text{\AA}$), $\alpha\text{-Al}_2\text{O}_3$ (trigonal, $R\bar{3}c$, $a = b = 4.75\text{\AA}$, $c = 12.98\text{\AA}$, $\alpha = \beta = 90^\circ$ and $\gamma = 120^\circ$), $\gamma\text{-Al}_2\text{O}_3$ (cubic, $Fd\bar{3}m$, $a = 7.91\text{\AA}$). The raw EBSD images were corrected in the direction normal to the sample surface to take into account the experimental tilt error of the EBSD sample preparation and measurement. The TKD measurements were performed using a 30 keV accelerating voltage at a working distance of 2 mm while the FIB lamellas were tilted 20° away from the detector to improve spatial resolution [30].

2.2.4. TEM analysis

After the TKD measurements, High Angle Annular Dark Field (HAADF) Scanning Transmission Electron Microscope (STEM) imaging, Energy Dispersive X-ray Spectroscopy (EDS) maps and Transmission Electron Microscope (TEM) analysis were carried out using an FEI Talos F200A instrument operated at 200 kV. The previously collected TKD phase maps allowed for specific grain boundaries to be studied.

2.2.5. SEM and EDS analysis

Using the FEI Helios P-FIB electron imaging capabilities, the surfaces of as-deposited oxide layers were observed using secondary electron imaging after the deposition of a thin Au-Pd conductive layer. Back-Scattered Electron (BSE) images of the cross-sections were also collected to measure the thickness of the oxide layers and to quantify porosity after binarisation using ImageJ software [31] (see Fig.S2 in Supplementary Materials available in the on-line version of this article). Finally, the coating chemical composition and elemental maps were obtained using an Oxford Instruments X-Max EDS detector at 15 kV. The

average elemental composition was acquired from a square area fitted to the coating thickness. The quantification was accomplished using the internal standards of Oxford Instruments' AZtec software.

2.2.6. Glow discharge optical emission spectroscopy (GDOES)

Complementary elemental depth profiling of the oxide layers was also investigated by GDOES, using a GD-Profilier 2 (Horiba Jobin Yvon) at Ar pressure of 635 Pa and a power of 35 W. A standard set of wavelengths was employed for element detection. Since the GDOES profiling signal has no strong spatial links to the specimen geometry, potassium concentration peaks at the surface and metal/oxide interface correlated in both GDOES and EDS line scans were used to estimate positions of the other GDOES profiles along the coating cross-section.

3. Results

3.1. Transition from PEO to post-sparking anodising

In the potentiostatic PB PEO mode, both positive and negative currents change reflecting non-stationary coating growth and corresponding structural transformations. Fig. 1a shows a typical evolution of the two current densities and associated current ratio R for the central point ($U_{\text{pos}} = 500\text{ V}$, $U_{\text{neg}} = -240\text{ V}$) of the 3^2 -factorial experiment. Following the initial voltage ramp, j_{Neg} and j_{Pos} behaved asynchronously in the potentiostatic step, first increasing and then decreasing, after 2.5 and 5 min, respectively. This led R to peak at ~ 2.1 between 1 and 2 min and then decrease promptly to ~ 1.7 , after about 5.5 min, after which it remained approximately constant. The asynchronous current behaviour is consistent with the formal description of anodic and cathodic

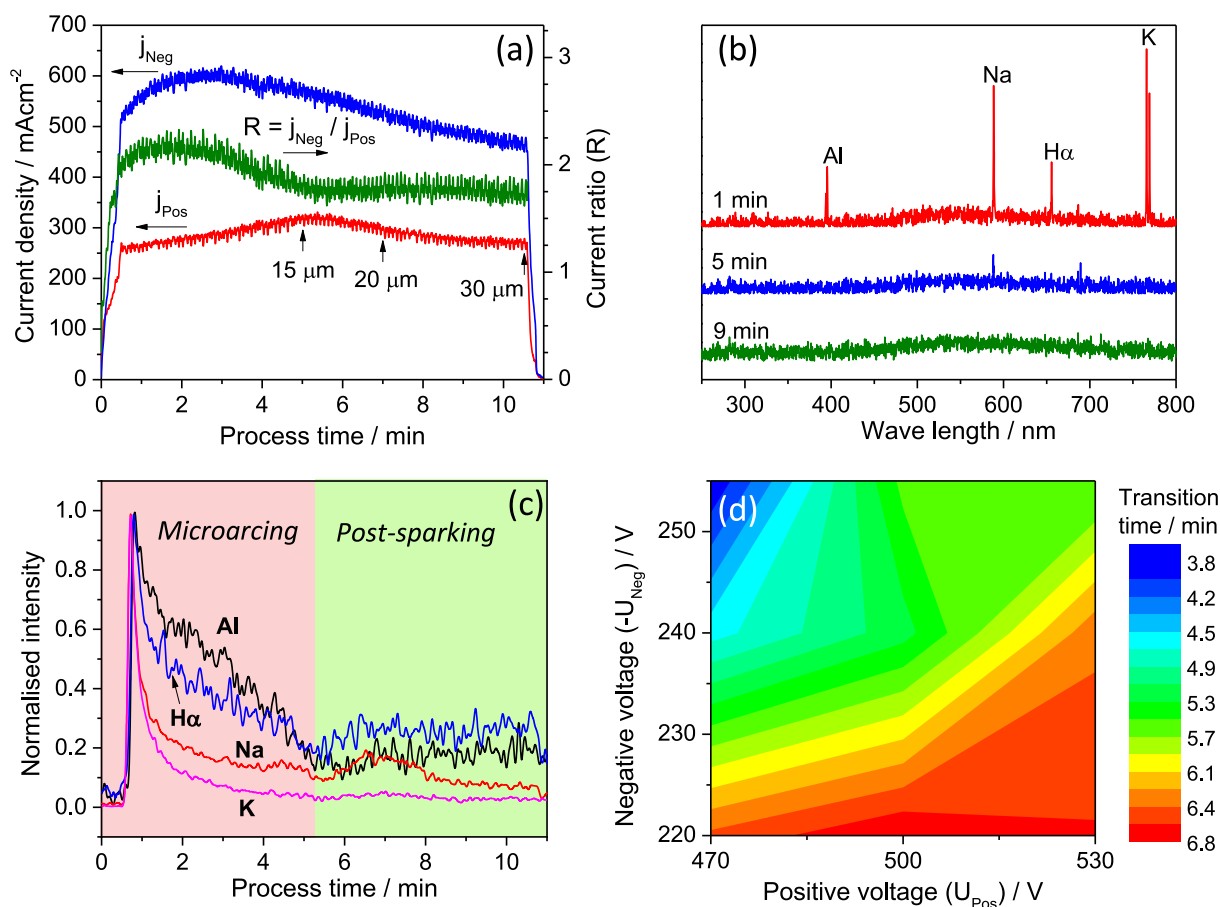


Fig. 1. Sustainability monitoring of PEO process: (a) Temporal evolution of current densities and R factor during potentiostatic treatment of Al alloy (+500/-240 V); (b) Examples of OES spectra collected at different stages of the process; (c) Evolution of atomic line peak intensities with processing time indicating transition to the post-sparking anodising stage; (d) Time to post-sparking transition as a function of positive and negative voltage set points.

processes in PEO Al by two different equivalent circuits [32]. A rather modest change in j_{pos} is different from that in the DC PEO process [33] where current drops down significantly to a minimum (leakage current) value limiting the final coating thickness. This indicates an influence of prior cathodic polarisation on effective conductivity of the barrier part of surface oxide in the positive direction, which enables thicker coatings to be grown more efficiently [13,25,26].

Unlike soft-sparking PEO, transition to the post-sparking stage is identified by the complete disappearance of atomic lines in the OES spectra (Fig. 1b,c). Seeming increases in intensities of H and Na lines after the transition are due to continuous galvanoluminescence within the 430 to 680 nm band common to anodising in inorganic electrolytes [34,35]. The incubation period for the transition varies smoothly within the studied voltage range between approximately 4 and 7 min (Fig. 1d), which is significantly shorter than the transition to soft sparking under galvanostatic control [13,25,26]. This means that the post-sparking mode is sustainable and can be implemented over a wide window of processing parameters, without falling into a destructive arcing regime or impeding coating growth, which is beneficial for scaling up the process.

3.2. Oxide layer morphology

To study the evolution of coating morphology during post-sparking PEO treatment, three oxide layers with thicknesses ~15, 20 and 30 μm were manufactured by processing the Al alloy substrates for 5, 7 and 11 min, at the central point of experiment (+500/-240 V, see Table 1). SEM images of the surface morphology (Fig. 2I) reveal nodular features typical of PEO coatings on Al. However, unlike oxide layers formed in conventional PEO mode, neither these features nor surface roughness (Table 1) change with coating thickness. This implies that beyond the initial sparking stage, the coating growth occurs mainly at the metal/oxide interface, i.e. 'reformative growth' via discharge channels reverts back to 'laminar growth' dominated by ionic migration across the oxide layer, similar to conventional anodising.

On BSE micrographs of the P-FIB cross-sections (Fig. 2II), all three coatings appear uniform and mostly dense. Increased porosity is present in the outmost region of the surface layer and, to a lesser extent, at the metal/oxide interface (Fig. 2II), whereas in the middle part, porosity is mostly below 5%. A network of cracks (not accounted for in porosity measurements) that may be interconnected propagating throughout the oxide layer [36] was also observed.

3.3. Oxide layer composition

3.3.1. Phase composition

According to XRD patterns (see Fig.S3 in Supplementary Materials available in the on-line version of this article), the 15 μm thick oxide layer contains only $\gamma\text{-Al}_2\text{O}_3$ phase while those with thickness 20 and 30 μm , have both γ and α phases present. This is consistent with the results of EBSD analysis (Fig. 2III) revealing α -phase bands in the inner parts of the latter two coatings, whereas the thinnest oxide contains only gamma phase albeit with a slightly larger grain size (Fig. 2IV). The fact that the $\alpha\text{-Al}_2\text{O}_3$ phase appears once the coating thickness exceeds a certain threshold is known; however this usually occurs at much greater thicknesses, e.g. above 50 to 60 μm , for conventional PEO coatings formed by 50 Hz AC polarisation [10].

Table 1

Morphological characteristics of studied oxide layers.

Sample code	Process duration / min	Average thickness / μm	Average surface roughness, Ra / μm
15 μm	5	15.0 \pm 0.3	0.65 \pm 0.11
20 μm	7	20.7 \pm 0.7	0.71 \pm 0.11
30 μm	11	30.2 \pm 0.9	0.60 \pm 0.10

Four regions can be distinguished in the heterophase oxide layers (Fig. 2III): an outmost layer (1) consisting of γ phase, an α -rich intermediate region (2), a γ -rich region near the metal/oxide interface (3), and finally a thin interfacial layer (4), where neither alpha nor gamma structure could be identified with confidence at this stage (details of this structure revealed at a higher magnification observation (Fig. 5) will be discussed in Section 3.4). The heterophase part of the coating formed by groups of equiaxed α grains (yellow grains in Fig. 2III) separated by protrusions of γ phase expands as the layer grows. The α -rich region could be associated with specific conditions for nucleation and growth of the alpha phase. The maximum grain size distributions for the α and γ phase are depicted in Fig. 2IV. Before phase transition, the grain size of the γ matrix tends to increase from the interface towards the surface indicating a trend for grain growth as the layer thickens with time. Appearance of the α phase (yellow bars in Fig. 2IV) coincides with a reduction in the size of γ grains within the heterophase region, with the location of largest α grains corresponding to the smallest size of γ grains.

3.3.2. Elemental composition

All the coatings comprise mainly O and Al as well as small amounts of the main alloying elements (0.2 to 0.5 at.% of Si and Mg, see Table S1 in Supplementary Materials available in the on-line version of this article). The EDS line scans (Fig. 2V) show that Mg, Mn and K tend to segregate towards the coating surface, and this effect is amplified as the oxide layer grows. GDOES profiles (Fig. 3) reveal uniform distributions of minor coating elements, whereas K tends to follow the porosity distribution (Fig. 2II), with higher concentrations at the coating surface and the metal/oxide interface, but lower content in the bulk of the oxide. This indicates that open porosity and microcracks may permit electrolyte ingress to the metal/oxide interface, thus sustaining the oxidation process without the need for destructive discharge events. Consistent with the EDS line scans, GDOES profiles for Mg show signal increasing towards the coating surface, while that of Si demonstrates generally opposite trend, with a minor increase in the near surface region, which can be accounted for by dissolution-precipitation of silicate species in the highly alkaline media [37]. Hydrogen is present throughout the oxide layer, decreasing from the surface to the bulk of the oxide and then forming a slight local maximum at the metal/oxide interface, indicating a possible presence of hydrated phases within the interfacial barrier layer, where the oxide is initially formed.

3.4. Preferred orientations and orientation relations between grains

The inverse Pole Figure (IPF) maps (Fig. 4) derived from the EBSD scans confirm the absence of any pronounced texture in the studied coatings, which is consistent with nearly equiaxed grain shapes for both phases. However, a slight preferred orientation can be noted in the 20 μm layer (Fig. 4b,e), wherein the α grains have their c-axes aligned roughly towards the coating surface plane (20 to 40° away) and the γ grains have their [111] and [001] axes roughly towards the surface (14° away). The IPF results presented in Fig. 4 are overlaid upon the band contrast (BC) maps which represent the pattern quality at each point (along a grey scale from black to white for low to high pattern quality). The high quality of the Kikuchi patterns can be observed by the overall lightness of Fig. 4a-c within both the substrate and coating regions. However, a darker band can be seen along the metal/oxide interface indicating a lower quality indexing in the region of the thin amorphous/nanocrystalline interfacial layer.

To understand how the γ to α phase transition in PEO alumina occurs, TEM imaging and TKD mapping of the samples were undertaken. Results presented in Fig. 5a,b indicate that the transition does not change the type of microstructure. This is consistent with IPF maps presenting similar recrystallised equiaxed grain structures with increasing grain sizes from the metal/oxide interface to the coating surface (see Fig. 2IV and Fig. 4). In both cases, seemingly amorphous interfacial barrier layers could be observed. However, a high resolution TKD map (Fig. 5c, 5 nm

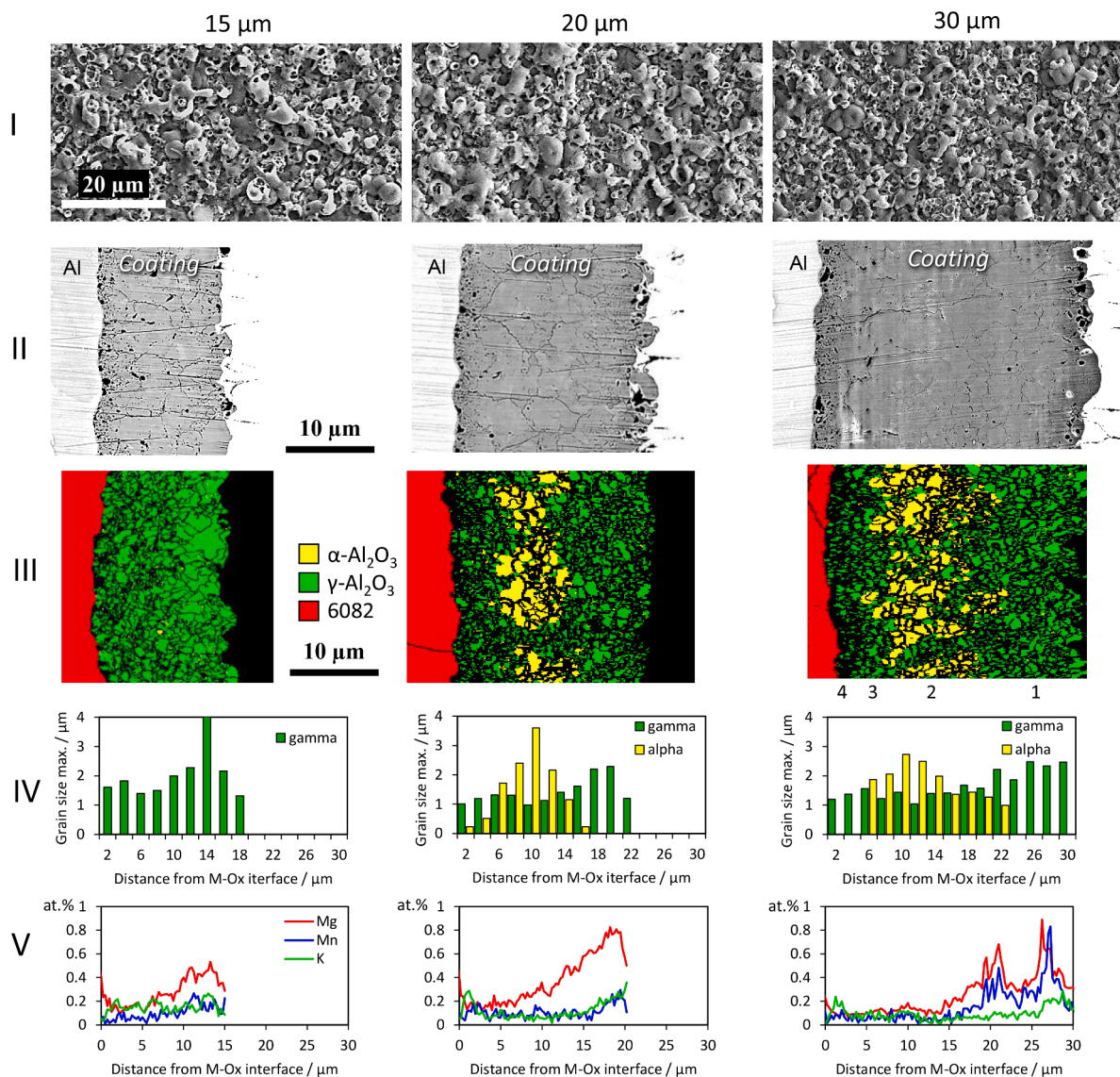


Fig. 2. Coating characterisation as a function of coating thickness: Panel I – Surface plane SE SEM images of oxide layer with various thicknesses; Panel II – BSE SEM images of P-FIB cross-sections; Panel III – EBSD phase maps representing the distribution of $\gamma\text{-Al}_2\text{O}_3$ (green), $\alpha\text{-Al}_2\text{O}_3$ (yellow) and the 6082 alloy (red); Panel IV – distribution of maximum grain size (equivalent diameter in μm) across the coating thickness obtained from IPF data (Fig. 4); Panel V – EDS line scans for impurity elements.

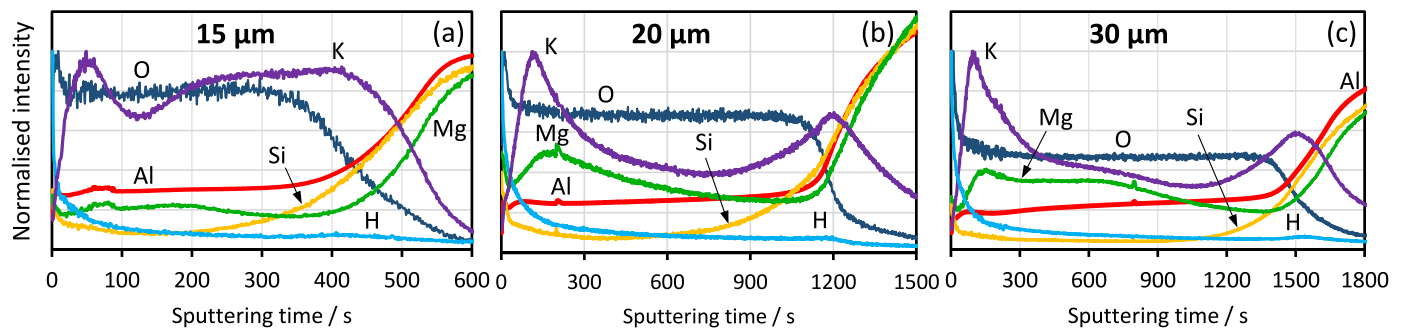


Fig. 3. GDOES profiles for the components of oxide layers of various thicknesses.

step size) and the dark field STEM image (Fig. 5d) reveal that the continuous barrier layer, having a thickness of about 200 nm and separating the interfacial porous oxide from the metal substrate, contains nanocrystalline inclusions (annotated with arrows, Fig. 5c).

Local misorientation maps show significant local misorientations between oxide grains both before and after $\gamma \rightarrow \alpha$ transition (Fig. 5a,b, ‘TKD Loc. Misor.’). However, in the 20 μm thick heterophase layer, a region with relatively low local misorientation can be identified as

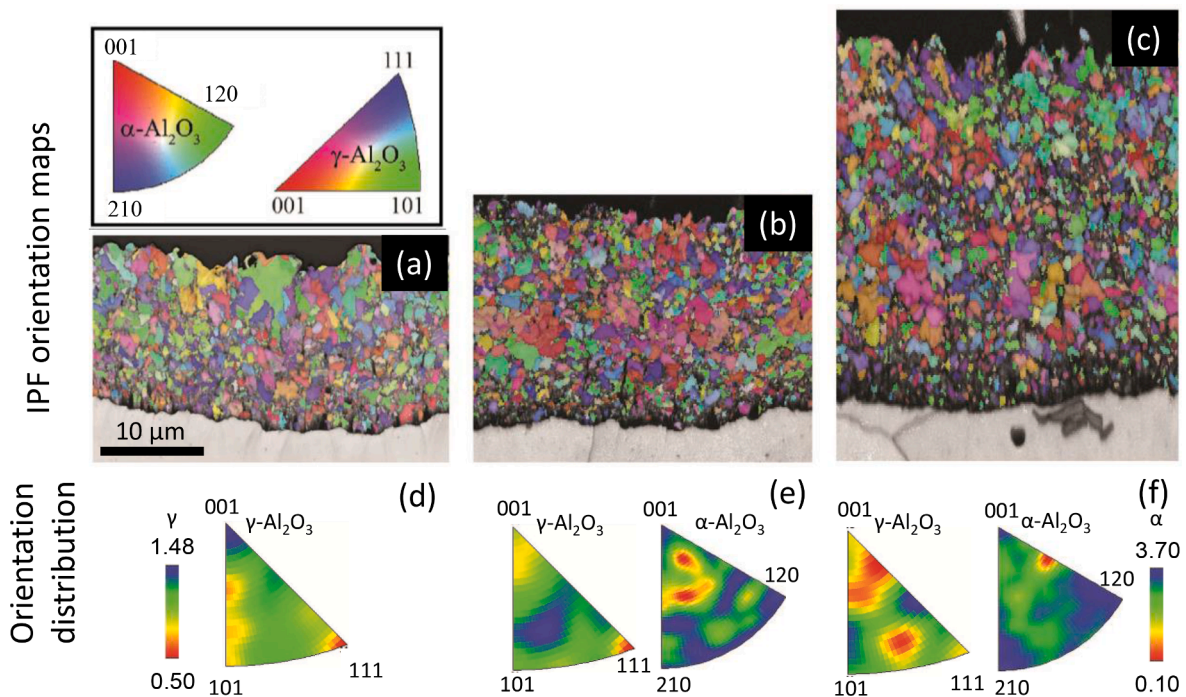


Fig. 4. EBSD IPF+BC maps representing grain orientations in the studied oxide layers: (a) 15 μm ; (b) 20 μm ; (c) 30 μm and corresponding equal area projections (d-f), upper hemisphere, half width 10° , cluster size 5° . Vertical bars depict range in units of spatial frequency both for gamma and α grains. For as-collected BC maps and associated histograms, please refer to Fig.S4 in Supplementary Materials available in the on-line version of this article.

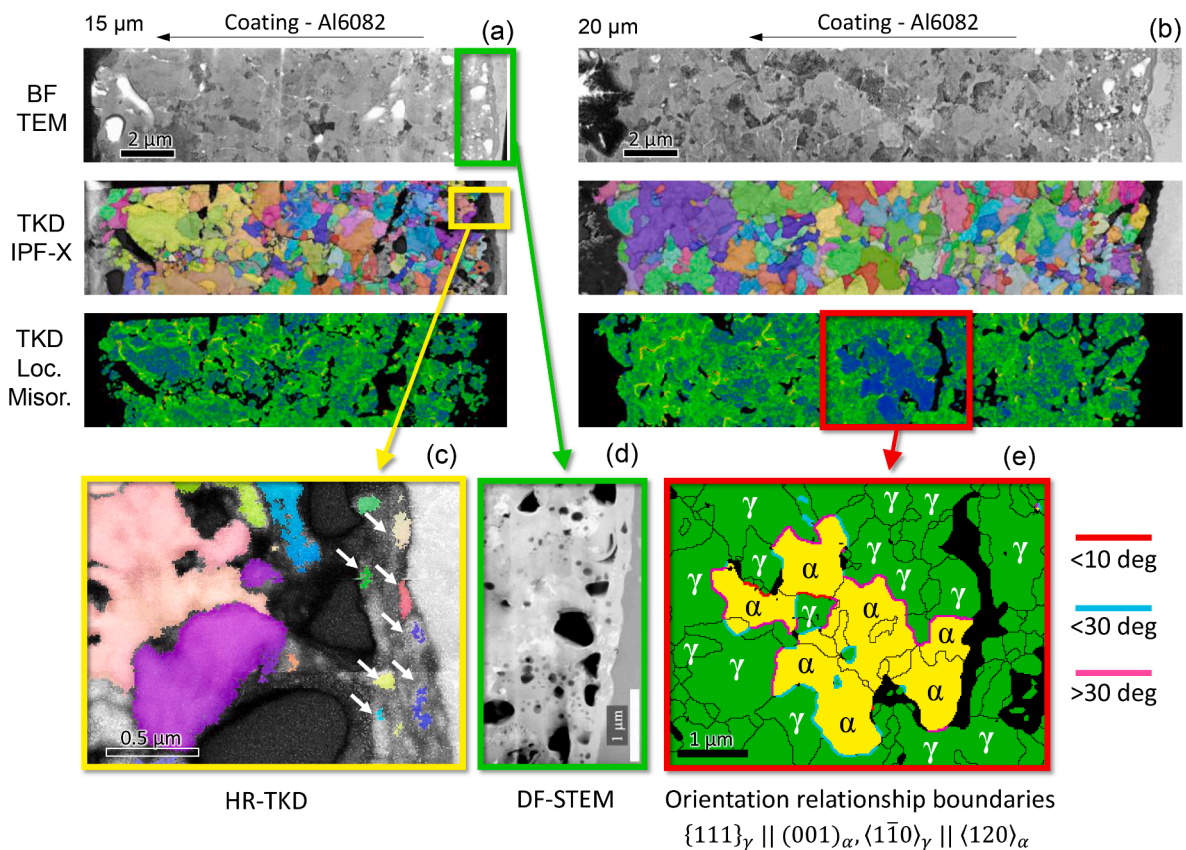


Fig. 5. Cross-sections of (a) thin and (b) thicker oxide layers before and after the $\gamma \rightarrow \alpha$ phase transition is triggered, respectively. Top to bottom: TEM Bright Field, TKD IPF+BC in the growth direction and TKD Local Misorientation map (0 to 2.5°); (c) High resolution view (HR TKD) of the metal/oxide interface in the 15 μm γ alumina layer with arrows denoting nanocrystals nucleated in the amorphous barrier layer; (d) Dark field STEM image of the metal/oxide interface; (e) TKD Phase map of the 20 μm thick oxide layer with highlighted $\{111\}_\gamma \parallel (001)_\alpha$, $\langle 110 \rangle_\gamma \parallel \langle 120 \rangle_\alpha$ orientation relationships between α and γ phase boundaries. For as-collected BC maps and associated histograms, please refer to Fig.S5 in Supplementary Materials available in the on-line version of this article.

denoted by the red frame in Fig. 5b. This was mainly attributed to the misorientation within α grains (0.25° average) as confirmed in the phase map (Fig. 5e), while the γ phase grains retained on average more than twice the local misorientation (0.55°).

The orientation relationships $\{111\}_\gamma \parallel \{001\}_\alpha$, $\langle 110 \rangle_\gamma \parallel \langle 120 \rangle_\alpha$ at the γ/α grain boundaries were examined, as illustrated in Fig. 5e. Only a few of these boundaries deviate from the expected relationships by less than 10° and the most frequent deviations range between 20° and 50° , confirming the observation from the large scale EBSD maps (Fig. 4). This, together with significantly lower misorientation of α grains, indicates that formation of the alpha phase in this region is unlikely to be guided by parent gamma grain orientation.

3.5. Distribution of alloying elements

Apart from Al and O, PEO coatings on Al alloys often include minor amounts of substrate alloying elements whose distribution in the oxide layer is influenced by their solid-solution solubility and cationic mobility in the alumina matrix. The $\gamma \rightarrow \alpha$ transition in PEO alumina may cause redistribution of these impurities as both their solubility and mobility in these phases will differ. Fig. 6 provides STEM, TKD and EDS maps of the alpha-rich zone in a plane parallel to the metal/oxide interface extracted from the 30 μm thick oxide sample (see Fig.S1c in Supplementary Materials available in the on-line version of this article).

For the γ/α grain boundary shown in Fig. 6b, the gamma grain

appears to be enriched in Mg with its concentration increasing towards the boundary (Fig. 6d), whereas adjacent α grains are lean in Mg. At the same time, Mg segregation is not detected at α/α or γ/γ boundaries. In addition to Mg being mainly confined within the gamma grain, increased concentrations of Fe, Mn, Mg and, to a lesser extent, Si can also be observed at the grain boundary (Fig. 6e-g). Moreover, nanosized precipitates containing Fe, Mn and Si (indicated by arrows in Fig. 6b) are prominent around the intergranular void formed at the γ/α grain boundary. The intergranular voiding and cracks (dark regions in Fig. 6a) could be due to shrinkage during phase transformation arising from the smaller molar volume of the α phase compared to γ .

Another interesting observation is the bowing of the α/γ grain boundary around a small intragranular Mg-Fe impurity indicated by yellow circle in Fig. 6c. This suggests that the stable inclusion formed within the γ grain may have prevented the propagation of the α phase. Unlike intergranular gaps with precipitates observed previously, the two phases appear to be in an intimate contact at this boundary which is formed in the region with low concentration of impurities, so that only traces of elemental segregation can be seen at the interfacial region within the γ grain (Fig. 6h-k).

4. Discussion

The layered structure of the PEO coating has been first considered at the early stages of development of AC PEO technology, to account for

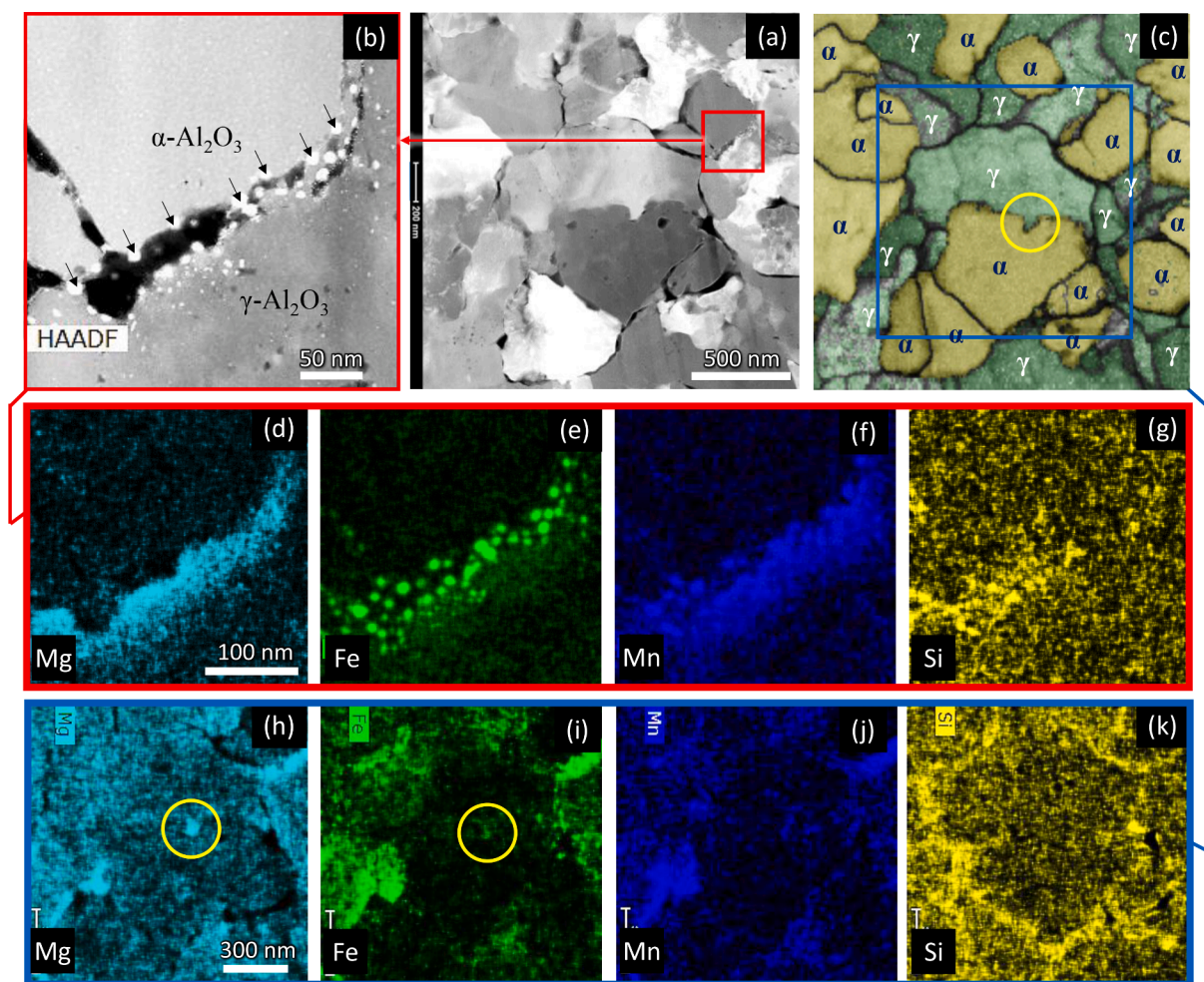


Fig. 6. Elemental segregation at α/γ phase boundaries in the α -rich region of the 30 μm thick oxide layer: (a) HAADF-STEM image across multiple grains; (b) HAADF-STEM image illustrating nanoparticle precipitation at γ/α grain boundaries; (c) TKD+BC phase map; (d-g) EDS elemental maps of an impurity rich α/γ grain boundary shown in (b); and (h-k) EDS elemental maps of the region in (c) showing a low impurity α/γ grain boundary bowed around a small Mg-Fe precipitate (circled). For the as-collected BC map and associated histogram, please refer to Fig.S6 in Supplementary Materials available in the on-line version of this article.

the non-uniform wear rate, microhardness and porosity [16,38] as well as phase distribution evaluated by layer-by-layer XRD analysis [39,40]. It was found that the maximum microhardness and alpha phase content were displaced from the metal/oxide interface by 5 to 20 μm [41–46]. These findings were confirmed with a higher accuracy in more recent studies [19,47–50]. Although phase segregation in PEO coatings has been known for a long time, the question as to its origin is unresolved. In this work, two types of segregation have been observed: (i) segregation of alumina polymorphs across the coating thickness and (ii) impurity segregation accompanying the $\gamma \rightarrow \alpha$ transition.

The $\gamma \rightarrow \alpha$ phase transition in alumina can be affected by various factors such as temperature, impurities, crystal size, electric field, internal stress or pressure [3]. The location of alpha-rich bands suggests that the necessary and sufficient conditions for this transition are fulfilled only within a certain coating region. However, all reactions involved, including substrate oxidation and monotropic phase transitions, are exothermal, and the external electric field is necessary only to overcome activation energy in the overall reaction pathway [51]. The transition from the cubic γ to the trigonal α structure is reconstructive [52], i.e. it requires the 3D rearrangement of both anion and cation sub-lattices including impurities, therefore the activation energy for this process is high (5.0 to 5.2 eV) [53]. Considering the size of α grains ($D^\alpha = 2.0 \dots 3.5 \mu\text{m}$, Fig. 2IV, 20 μm) formed over a relatively short period of time ($t \approx 2 \text{ min}$, Fig. 1a), it is likely that the transition consumed most of the parent γ grains and is controlled by the mobility of grain boundaries. From the above data, the velocity of the grain boundaries, estimated as $D^\alpha/2t$, can be inferred to be of the order of 10 nm s^{-1} , which corresponds to an effective temperature of at least $1200 \text{ }^\circ\text{C}$ [53]. This is unlikely to be the actual temperature sustained in such a close proximity to the Al substrate for any significant period of time without causing any noticeable damage to it (Fig. 4a-c). Therefore, thermal activation appears not to be the sole mechanism enabling the α grain growth, and field assisted migration and dissolution-precipitation mobility routes should also be taken into account.

4.1. The $\alpha\text{-Al}_2\text{O}_3$ band generation mechanism

Apart from the effects of pressure on alumina phase formation [54, 55], the influence of anodising temperature on phase composition is well known. Hard anodising is typically carried out at sub-zero temperatures leading to the formation of amorphous oxide films with a thickness similar to that of the PEO coatings studied here [56]. At the same time, the formation of thinner α -alumina containing anodic films has been reported in molten salt baths, under moderate heating to $150\text{--}200 \text{ }^\circ\text{C}$ which is much lower than the $800\text{--}900 \text{ }^\circ\text{C}$ required for initiation of the $\gamma \rightarrow \alpha$ transition in bulk ceramics [57–59].

In the absence of apparent discharge events and associated conductive microchannels during the post-sparking anodising stage, the electric field (E) developed under anodic polarisation can be considered uniform along the surface plane and non-uniform in the direction of the growing oxide layer [14,32]. Hence the system can be reduced to a simple 1D model, wherein in the main voltage drop occurs in the ‘active zone’ leading to a local increase in E near the metal/oxide interface, where the anodic reaction resulting in oxide formation takes place leading to the barrier layer being continuously renewed (Fig. 7a). This is supported by results of *in situ* impedance measurements showing that the barrier layer provides the largest resistance to charge transfer during both conventional anodising [60] and the PEO process [61]. The field remains relatively low through the remainder of the coating, termed the ‘product zone’ by analogy with a Plug Flow Reactor (PFR) in chemical engineering. While $\alpha\text{-Al}_2\text{O}_3$ is chemically inert and dielectric, $\gamma\text{-Al}_2\text{O}_3$ may be hydrated, which will increase its conductivity, thereby reducing E in the gamma-rich regions of the coating. The α enriched region having a lower conductivity and reduced effective cross-section of more conductive phases would then provide a small local increase in electric field, as denoted by the dashed line in Fig. 7a.

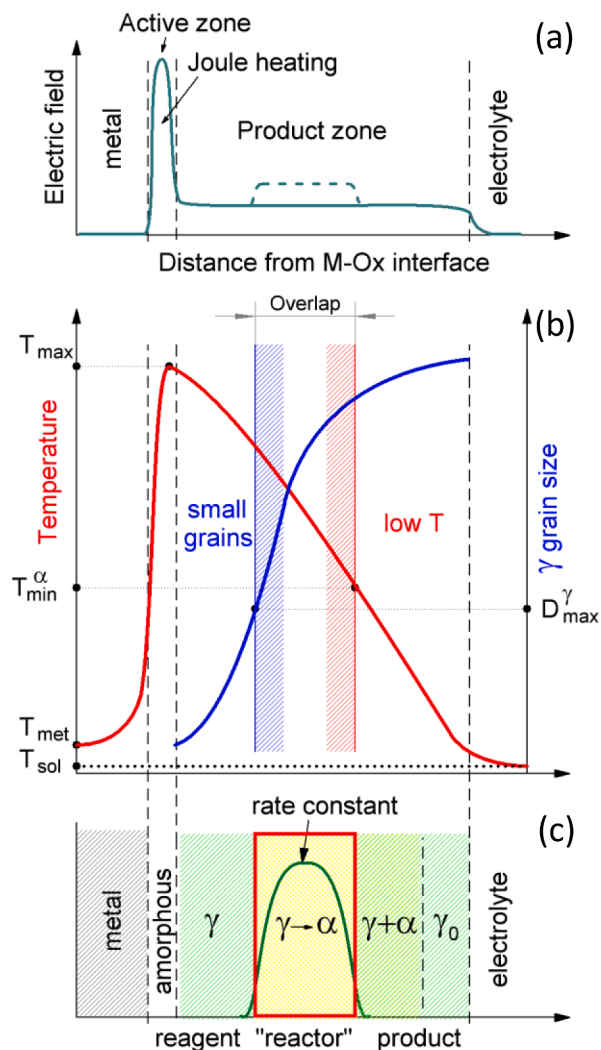


Fig. 7. Schematic illustration of the distributions in the oxide layer under anodic polarisation: (a) Electric field, (b) Temperature and γ -phase grain size and (c) Phase composition.

A high field in the narrow active zone leads to significant energy dissipation (Joule heating) within this region. The fact that Joule heating has been found to be the main source of heat during anodic processing [62,63] and observations of substrate temperature being noticeably higher than the surrounding electrolyte [64,65] support this argument. The temperature profile within the oxide layer can therefore be schematically depicted as shown by red line in Fig. 7b, with a maximum at the Joule heat source. Assuming that the thermal field alone provides the essential condition $T > T_{\min}^\alpha$ for the $\gamma \rightarrow \alpha$ transition, both the appearance of $\alpha\text{-Al}_2\text{O}_3$ in the inner part of the coating and the presence of the outer region composed of only $\gamma\text{-Al}_2\text{O}_3$ phase ($T < T_{\min}^\alpha$) can be explained. However, such a temperature distribution cannot explain the existence of a broad $\gamma\text{-Al}_2\text{O}_3$ region beneath the $\alpha\text{-Al}_2\text{O}_3$ band, where the temperature is expected to be close to T_{\max} .

Crystallisation of amorphous alumina proceeds by a nucleation and growth mechanism. During this process, gamma phase which is thermodynamically metastable in a bulk form usually appears before $\alpha\text{-Al}_2\text{O}_3$ because of its lower activation energy barrier for nucleation [66]. Due to the contribution of surface energy, fine γ grains remain thermodynamically favoured if their size is smaller than a certain critical size, D_{\max}^γ [67,68]. Therefore, the condition $D > D_{\max}^\gamma$ becomes sufficient for the $\gamma \rightarrow \alpha$ transition to actually occur at any coating location, where the essential condition ($T > T_{\min}^\alpha$) is satisfied.

Our observations show that initially, the γ phase nucleates within the amorphous barrier layer formed at the metal/oxide interface (see nanocrystalline grains in Fig. 5b). This can explain the absence of an apparent orientation relationship with the underlying Al grains and significant misorientation between the gamma grains observed in EBSD maps (Fig. 4). The porosity band at the interfacial barrier layer (Fig. 2II) may preserve the fine gamma grains from enlargement. The origin of this band can be attributed to thermally induced dehydration of the primary amorphous hydrated alumina [32] with release of water vapour and formation of gamma aluminium oxide: $2\text{Al}(\text{OH})_3(\text{s}) = \gamma\text{-Al}_2\text{O}_3(\text{s}) + 3\text{H}_2\text{O}(\text{g})$. From the EBSD maps (Fig. 2IV), the size of the $\gamma\text{-Al}_2\text{O}_3$ grains tends to increase from the metal/oxide interface towards the coating surface. This may be due to recrystallisation via a hydrothermal dissolution/precipitation mechanism which provides a trend opposite to the temperature distribution in the oxide layer, as illustrated by blue line in Fig. 7b. Considering the temperature and grain size distributions, there appears a region in the central part of the coating, where both conditions, $T > T_{\text{min}}^{\alpha}$ and $D > D_{\text{max}}^{\gamma}$, are met, and so the $\gamma \rightarrow \alpha$ transition will occur there, at a sufficient rate (Fig. 7c).

4.2. Elemental redistribution during phase transition in PEO alumina

4.2.1. Impurity effects on the $\alpha \rightarrow \gamma$ transition

The phase composition and the associated properties of PEO coatings can be influenced significantly by the alloying elements present in the metal substrate. Thus, in PEO coatings formed on Al alloys with Zn (7xxx series), the amount of $\alpha\text{-Al}_2\text{O}_3$ is significantly lower while the total coating thickness and oxide formation efficiency remain similar to those on 6xxx series alloys [40,50,69]. The presence of up to a few percent Si [40,70], Mg [71,72], Mn [73] and Sn [74] in Al alloys does not affect alpha phase formation in the corresponding PEO coatings, but higher concentrations of those elements become detrimental. An opposite trend is observed for Cu which may promote $\alpha\text{-Al}_2\text{O}_3$ formation up to at least 10 wt.% [75]. To the best of our knowledge, until now no comprehensive explanation has been provided as to the effects of alloying elements on phase composition of PEO alumina, although changes in specific conductivity of oxide [75], its melting point [70,74], and coating porosity [72] were considered as possible influencing factors.

The thermodynamically favourable $\gamma \rightarrow \alpha$ phase transition in alumina follows zero order kinetics [76] which can be controlled by impurities, at least for electrochemically grown alumina. The impurities (as individual or mixed oxides) can be classified into three groups according to their effect on the transition to the α phase:

- Inhibitors (Ca, Sr, Ba, La, Ce, Zr, Si) [77–82];
- Neutral (Co, Ni, Mg) [77,83];
- Promoters (Cu, Cr, Mn, Fe, Si) [77,82,84–86].

Inhibition is normally associated with stabilisation of a certain transition alumina polymorph and can be accounted for by occupation of vacancies in the cationic sub-lattice which collapses during the normal $\gamma \rightarrow \alpha$ transition, thereby preventing reconstructive lattice rearrangement as additional diffusion is required [87]. Promotion is explained by different mechanisms. For impurities that form oxides with lattices isostructural to $\alpha\text{-Al}_2\text{O}_3$ (e.g. $\alpha\text{-Fe}_2\text{O}_3$, Cr_2O_3), critical α nuclei can be formed at significantly lower temperatures [86,88]. For Cu and Mn additives, this sometimes is also attributed to the formation of a liquid phase at temperatures below the normal $\gamma \rightarrow \alpha$ transition [81]. Additionally, crystalline SiO_2 is known to promote the $\gamma \rightarrow \alpha$ transition, whereas amorphous silica inhibits it [82].

In the 6082 Al alloy employed in this work, the main alloying element, Mg, is considered to be a neutral or slightly accelerating impurity [80]. However, oxides of Fe and Mn impurities are accelerators. Since the amounts of impurities are normally quite small, the effect of such doping is difficult to distinguish from pure $\gamma\text{-Al}_2\text{O}_3$ by conventional XRD techniques. However, taking into account the statistically defined

distribution of aluminium cations in the octahedral and tetrahedral sites of $\gamma\text{-Al}_2\text{O}_3$ spinel structure, the effect of an impurity X can be presented as formation of a solid solution with variable stoichiometry $\text{Al}_{2.67-X}\text{Y}_X\text{O}_4$ in the doped gamma phase (γ^X).

4.2.2. Effect of micro-segregation on alpha grain growth

Let us consider a model γ^X oxide grain with initial ('0') impurity X concentration $C_{X_0}^{\alpha} < C_{X_0}^{\gamma} < C_{X_{\text{max}}}^{\gamma}$ (Fig. 8a,b) located within the inner region of the coating, where the $\gamma \rightarrow \alpha$ transition is allowed (see Section 4.1). Here, $C_{X_{\text{min}}}^{\alpha}$ and $C_{X_{\text{max}}}^{\gamma}$ denote impurity solubility limits in α and γ phases, respectively. A nucleus of the $\alpha\text{-Al}_2\text{O}_3$ phase can form within the γ^X grain due to impurity content fluctuation. Once the nucleus reaches a critical size and becomes stable ('1'), segregation into an X-lean $\alpha\text{-Al}_2\text{O}_3$ core ($C_{X_{\text{min}}}^{\alpha}$) and an X-rich boundary with the γ matrix is formed after which steady α grain growth ('1 \rightarrow 2') will be established.

The steady state growth of the α grain may be interrupted for several reasons. Firstly, if $C_{X_0}^{\gamma}$ is relatively low, the whole γ grain may be transformed, and existing γ grain boundaries will become a natural obstacle for propagation of the new α phase. Secondly, in γ grains with a higher initial impurity concentration $C_{X_0}^{\gamma}$, the α/γ grain-boundary mobility can be impeded when the impurity concentration in the boundary layer reaches the solubility limit $C_{X_{\text{max}}}^{\gamma}$ (e.g. see Fig. 6d, X = Mg). At this point, the impurity oversaturated γ^X phase undergoes decomposition to the α phase (Fig. 8c, '3') and a new stable spinel phase Al_2XO_4 or AlXO_3 for divalent or trivalent impurities, respectively (Fig. 8c, '4'). Precipitation of the new phase forms a shell surrounding the α grain (see Fig. 8a, 'spinel shell'), which stops further propagation of the α/γ grain boundary. Thus, increased impurity concentration in the parent gamma grain can limit the size of $\alpha\text{-Al}_2\text{O}_3$ grain (Fig. 8b, D_{max}^{α}) even though it may be an impurity accelerating the $\gamma \rightarrow \alpha$ transition itself.

It is noteworthy that the above mechanism postulates two reaction pathways yielding $\alpha\text{-Al}_2\text{O}_3$:

- Steady state growth of the $\alpha\text{-Al}_2\text{O}_3$ grain by the $\gamma \rightarrow \alpha$ transformation accompanied with impurity segregation because of different solubility (path 1 \rightarrow 2):



- Spinel shell formation by spontaneous decomposition of the oversaturated γ^X phase (path 2 \rightarrow 3,4):



The primary reaction (1) is an interfacial conversion process limited by impurity diffusion taking place at the α/γ grain-boundary. The secondary reaction (2) is a spinodal-like decomposition of an oversaturated γ^X phase which is also metastable in respect to the $\gamma \rightarrow \alpha$ transition. As a result, formation of the primary α grain surrounded by a shell consisting of microcrystals of spinel and secondary α phase can be expected (Fig. 8d). Since the shell is thinner than the critical size of the α nucleus, secondary α grains are likely to coalesce with the primary α grain and only spinel particles can be identified at the boundaries (Fig. 6).

4.2.3. Effect of macro-segregation on oxide layer morphology

In addition to impurity micro-segregation, the proposed alpha band formation mechanism provides a plausible explanation for the macroscopic segregation of alloying elements across the oxide layer. Fig. 9a combines spatial distributions of coating porosity, local α/γ percentage and concentration profile of the main alloying element, Mg. Before the $\gamma \rightarrow \alpha$ transition, i.e. in the 15- μm thick coating, porosity and Mg concentration profiles overlap, and once the transition is triggered, the formed α -rich band inversely correlates with both porosity and impurity

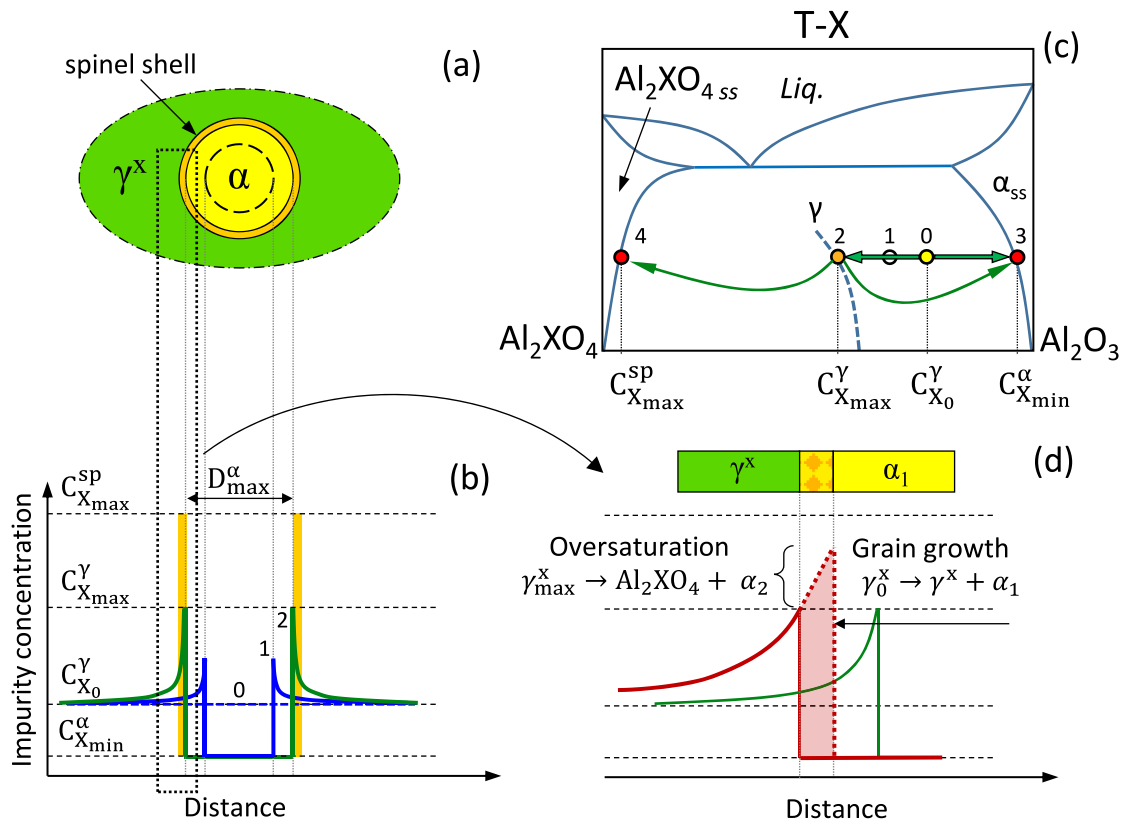


Fig. 8. (a) Schematic diagram of alumina grain undergoing $\gamma \rightarrow \alpha$ phase transition; (b) Impurity (X) concentration profiles within γ^x -phase during growth of an α crystal (see text). (c) Composition-temperature binary phase diagram for a spinel- Al_2O_3 system. Dashed γ line represents hypothetical non-equilibrium solubility limit of impurity X in metastable γ alumina; (d) A magnified view of the dotted area in panel (b) clarifying details of spinel shell formation. Not to scale.

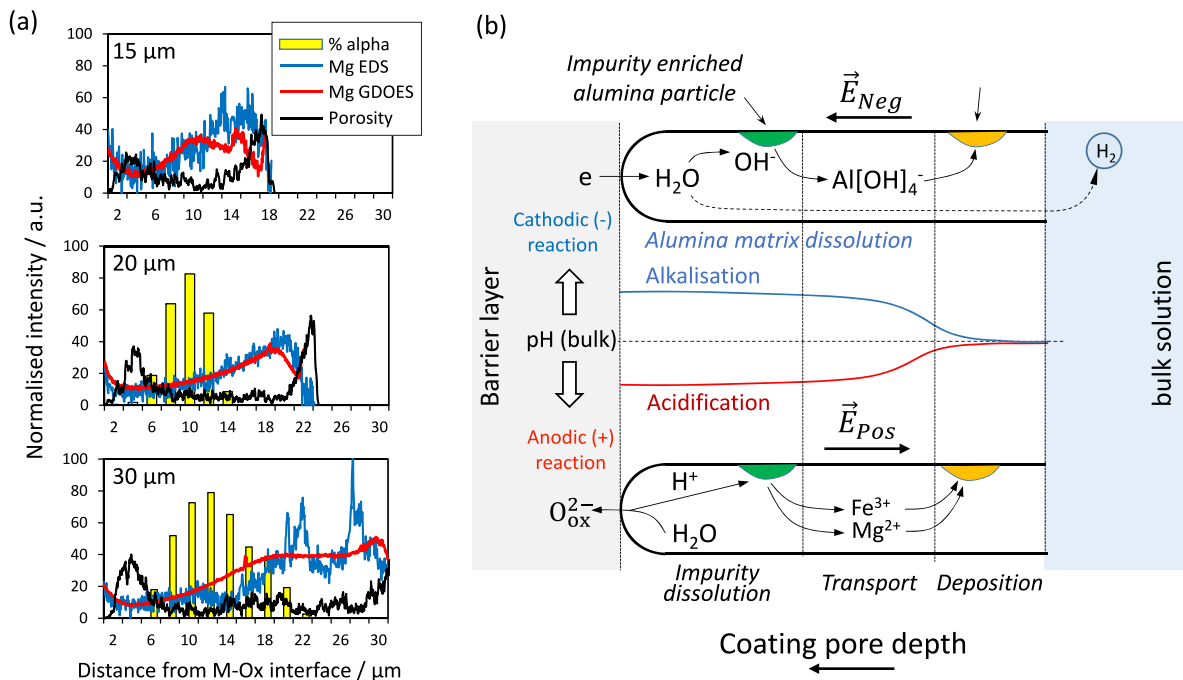


Fig. 9. (a) Combined distribution profiles of coating porosity, γ -, α -phase and impurity concentrations across studied oxide layers; (b) Schematic illustration of the effect of local pH changes on solubility of various species.

concentration profiles, in the 20 and 30- μm thick coatings.

The region of reduced impurity concentration in the inner part of the oxide layer widens as the coating grows, which could be linked to the micro-segregation induced by the $\gamma \rightarrow \alpha$ transition (Sec. 4.2.1). Impurities accumulated at the grain boundaries and in secondary phase nanoparticles formed at the intergranular voids (see Fig. 6b) may become mobile within the coating, through the interconnected pore network, via either particle migration or dissolution-precipitation mechanism. Under alternating polarisation, local electrolyte pH within the pores could deviate significantly from that in the bulk solution because of transport limitations (Fig. 9b). A combination of local pH favouring solubility with suitable electric field may drive dissolved species either outward or inward to/from the surface layer, depending on the speciation of soluble complexes and their charge. The same transport limitations within the porous structure will then lead to precipitation of insoluble compounds in other parts of the coating, where different local conditions (pH, temperature and composition) favour such precipitation.

4.3. Control over the coating phase composition

Summarising the discussion above, we propose an alternative model for the formation of α alumina in the surface layer during high-voltage anodising of Al alloys, which does not rely on cyclic melting-solidification of oxide micro-volumes by localised plasma discharges inherent to the conventional PEO process. According to this model, the region within the oxide layer, where necessary and sufficient conditions for $\gamma \rightarrow \alpha$ transition are fulfilled, can be represented by a solid-state analogy of the Plug Flow Reactor model (Section 4.1 and Fig. 10a). The performance depends on the input flow of the γ -phase (F) formed in the interfacial barrier layer and the temperature profile $T(x)$ in the coating that determine the kinetics of $\gamma \rightarrow \alpha$ transition. In the steady state approximation (slowly changing processing parameters), the temperature profile $T(x)$, dimension (L) and residence time in the reactor are constant.

The input flow F is controlled by the rate of coating mass gain, which is proportional to the current of the anodic reaction (I_{ox}) according to Faraday's law. Effective length and residence time are dependent on the temperature profile $T(x)$, which is controlled by the current of ionic transport (I_{loss}) which, in turn, determines heat dissipated in the oxide layer. Meanwhile, anodic charge transfer during the PEO process can be represented by a simplified equivalent circuit as in Fig. 10b (disregarding electrolyte resistance) [32,89]. This circuit consists of resistance to ionic transport in the film (R_{loss}) connected in series with an RC loop comprising capacitance of the electric double layer (C_{edl}) connected in parallel with resistance to the interfacial anodic reaction (R_{ox}). Both I_{ox} and I_{loss} are linked to corresponding equivalent circuit resistances via Ohm's law. Since the ratio of currents through C_{edl} and R_{ox} is frequency dependent (Fig. 10c), F and $T(x)$ parameters of the PFR are expected to

be affected by the frequency of alternating current polarisation in different ways. Thus, there is a frequency range, wherein the extent of $\alpha\text{-Al}_2\text{O}_3$ generation can be controlled (Fig. 10c, P_α), which can be used for optimisation of the phase composition of ceramic alumina formed in the post-sparking PEO stage.

Further control over the surface morphology and phase composition can be achieved by the application of potentiostatic polarisation which provides non-stationary oxide growth conditions, with an electric field across the surface layer reducing over time. This work has demonstrated that such conditions can provide a nearly constant oxide growth rate (Fig. 10d) similar to that achieved by conventional AC and PB PEO treatments under galvanostatic control (constant electric field). Apart from a dramatic acceleration of the transition to the post-sparking stage (4 to 7 min, Fig. 1d) leading to noticeable refinement of the coating morphology, a clear benefit of such an approach lies in the significant reduction of the incubation period (~ 5 min, Fig. 10d) required for the formation of critical-size alpha nuclei that enable the $\gamma \rightarrow \alpha$ transition. The incubation in reactive sintering of pressed Al_2O_3 ceramics at 1150 $^\circ\text{C}$ could take between 2 and 12 h [90] and up to 40 min in the state-of-the-art PEO processes [13,25,26]. Sigmoidal kinetics of the α phase growth observed following the incubation period (5 to 7 min, Fig. 10d) exceeds the total oxide growth rate, indicating that the $\gamma \rightarrow \alpha$ transformation occurs spontaneously. This is consistent with the proposed α band generation mechanism which relies on the specific temperature distribution and parent γ grain size dependent triggering of the phase transition in the solid state.

5. Conclusions

This work has demonstrated a process window for growing relatively thin (20 to 30 μm), yet dense, crystalline anodic oxides enriched with high-temperature $\alpha\text{-Al}_2\text{O}_3$ at near-to-ambient Al-alloy substrate temperatures. Formation of the $\alpha\text{-Al}_2\text{O}_3$ phase and morphological refinement of the crystalline γ alumina matrix were promoted by applying bipolar voltage pulses that led to a transient current response behaviour with variable ratio $R > 1$, resulting in prompt and complete suppression of the interfacial plasma discharge characteristic of conventional PEO treatments.

The α phase grains were formed spontaneously in the regions of crystalline anodic oxide where the appropriate temperature distribution and size of γ grains that are relatively free from impurities have been achieved, allowing sufficient mobility of α/γ grain boundaries. The mobility was assisted by migration of cationic impurities in the oxide layer sustained by their hydrothermal dissolution/precipitation and facilitated by concentration and pH gradients established within the microporous network permeable by electrolyte.

Due to increased ionic mobility, the critical temperature required for activation of the $\gamma \rightarrow \alpha$ transition in post-sparking anodising can be

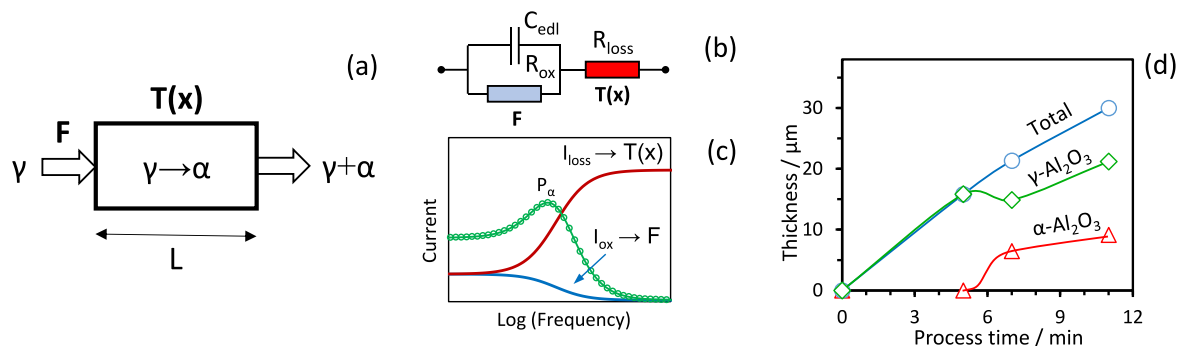


Fig. 10. (a) Schematic diagram of the Plug Flow Reactor model describing $\gamma \rightarrow \alpha$ phase transition during the PEO process, where F is input flow of γ phase, $T(x)$ is temperature profile along the reactor and L is effective reactor length; (b) A simplified equivalent circuit of anodic response of the PEO electrode; (c) Effect of pulse polarisation frequency on redistribution of anodic current via various routes and associated characteristics of the PFR reactor in quasi-potentiostatic regime; (d) Kinetics of α and γ phase contribution to the overall coating thickness during the PEO process.

reduced significantly compared to those in both reactive sintering of bulk alumina ceramics and conventional PEO processing of Al alloys, where such a transition is linked to the generation of micro-volumes of molten alumina by localised microdischarge events. This, together with shorter treatment times, minimises the risk of inflicting thermal damage to the metal substrate, which may be of particular concern for precipitation-hardened high-strength Al alloys. Moreover, the oxide layer growth and phase evolution in the post-sparking mode can be described by a simple quasi-stationary 1D PFR model which provides a useful framework for in-depth understanding of anodic oxides formation on light alloys by high-voltage electrochemical processing.

Data availability

All data supporting this study are provided in Section 3 ‘Results’ and Appendix ‘Supplementary Materials’ Raw data used for microstructural characterisation and microanalysis can be made available upon reasonable request.

Declaration of Competing Interest

The authors declare that they have no known competing financial interests or personal relationships that could have appeared to influence the work reported in this paper.

Acknowledgements

The research leading to this publication was supported by the UK EPSRC (grant EP/T024607/1) and the European Research Council (ERC AG 320879 – ‘IMPUNEP’ and ERC-2018-PoC 825122 – ‘3D Cer-Met’). E. B. would like to acknowledge the Canadian Natural Sciences and Engineering Research Council’s support through the Postdoctoral Fellowship program, and Professors Jolanta Sapięha and Ludvik Martinu for their support. The infrastructure enabling this research was provided by the Henry Royce Institute for Advanced Materials, funded through the UK EPSRC grants EP/R00661X/1, EP/S019367/1, EP/P025021/1 and EP/P025498/1 and is acknowledged with thanks. The authors wish to thank Dr. Thomas Schmitt for the kind help on the X-ray diffraction experiments and Dr Jack Donoghue for his assistance on the EBSD experiments. For the purpose of open access, the author has applied a Creative Commons Attribution (CC BY) licence to any Author Accepted Manuscript version arising.

Supplementary materials

Supplementary material associated with this article can be found, in the online version, at doi:10.1016/j.actamat.2022.118587.

References

- [1] I. Polmear, D. StJohn, J.-F. Nie, M. Qian, The Light Metals, in: Light Alloys, Elsevier, 2017, pp. 1–29, <https://doi.org/10.1016/B978-0-08-099431-4.00001-4>.
- [2] G.W. Critchlow, D.M. Brewis, Review of surface pretreatments for aluminium alloys, *Int. J. Adhes. Adhes.* 16 (1996) 255–275, [https://doi.org/10.1016/S0143-7496\(96\)00014-0](https://doi.org/10.1016/S0143-7496(96)00014-0).
- [3] P. Neufeld, N.K. Nagpal, R. Ashdown, M. Akbar, Crystallization of anodic Al₂O₃, *Electrochim. Acta* 17 (1972) 1543–1546.
- [4] I. Levin, D. Brandon, Metastable alumina polymorphs: crystal structures and transition sequences, *J. Am. Ceram. Soc.* 81 (1998) 1995–2012.
- [5] S. Tajima, M. Soda, T. Mori, N. Baba, Properties and mechanism of formation of alpha-alumina (Corundum) film by anodic oxidation of aluminium in bisulphate melts, *Electrochim. Acta* 1 (1959) 205–216.
- [6] S.D. Brown, K.J. Kuna, T.B. Van, Anodic Spark Deposition from Aqueous Solutions of NaAlO₂ and Na₂SiO₃, *J. Am. Ceram. Soc.* 54 (1971) 384–390.
- [7] V.I. Belevantsev, O.P. Terleeva, G.A. Markov, E.K. Shulepko, A.I. Slonova, V. V. Utkin, Microplasma electrochemical processes, *Prot. Met.* 34 (1998) 416–430.
- [8] A.L. Yerokhin, X. Nie, A. Leyland, A. Matthews, S.J. Dowey, Plasma electrolysis for surface engineering, *Surf. Coat. Technol.* 122 (1999) 73–93, [https://doi.org/10.1016/S0257-8972\(99\)00441-7](https://doi.org/10.1016/S0257-8972(99)00441-7).
- [9] F.C. Walsh, C.T.J. Low, R.J.K. Wood, K.T. Stevens, J. Archer, A.R. Poeton, A. Ryder, Plasma electrolytic oxidation (PEO) for production of anodised coatings on lightweight metal (Al, Mg, Ti) alloys, *Trans. IMF* 87 (2009) 122–135.
- [10] A.B. Rogov, A. Yerokhin, A. Matthews, The Role of Cathodic Current in Plasma Electrolytic Oxidation of Aluminum: Phenomenological Concepts of the “Soft Sparking” Mode, *Langmuir* 33 (2017) 11059–11069, <https://doi.org/10.1021/acs.langmuir.7b02284>.
- [11] V.N. Malyshev, Coating formation by anodic-cathodic microarc oxidation, *Prot. Met.* 6 (1996) 607–611.
- [12] A.V. Timoshenko, Y.V. Magurova, Application of oxide coatings to metals in electrolyte solutions by microplasma methods, *Rev. Metal. Madrid.* 36 (2000) 323–330.
- [13] F. Jaspard-Mécuson, T. Czerwicz, G. Henrion, T. Belmonte, L. Dujardin, A. Viola, J. Beauvir, Tailored aluminium oxide layers by bipolar current adjustment in the Plasma Electrolytic Oxidation (PEO) process, *Surf. Coat. Technol.* 201 (2007) 8677–8682, <https://doi.org/10.1016/j.surfcoat.2006.09.005>.
- [14] A.B. Rogov, Y. Huang, D. Shore, A. Matthews, A. Yerokhin, Toward rational design of ceramic coatings generated on valve metals by plasma electrolytic oxidation: the role of cathodic polarisation, *Ceram. Int.* 47 (2021) 34137–34158, <https://doi.org/10.1016/j.ceramint.2021.08.324>.
- [15] W. Gebarowski, S. Pietrzyk, Growth Characteristics of the Oxide Layer on Aluminium in the Process of Plasma Electrolytic Oxidation.pdf, *Arch. Metall. Mater.* 59 (2014) 407–411, <https://doi.org/10.2478/amm-2014-0070>.
- [16] G.A. Markov, O.P. Terleeva, E.K. Shulepko, Microarc and arcing methods of protective coating deposition, *Proc. Gubkin’s MINH&GP* (1985) 54–64.
- [17] Y.V. Magurova, A.V. Timoshenko, The effect of a cathodic component on AC microplasma oxidation of aluminium alloys, *Zashchita Metallov* 31 (1995) 414–418.
- [18] A.V. Timoshenko, Y.V. Magurova, Microplasma oxidation of alloy of Al-Cu system, *Prot. Met.* 31 (1995) 523–531.
- [19] W. Xue, Z. Deng, Y. Lai, R. Chen, Analysis of phase distribution for ceramic coatings formed by microarc oxidation on aluminum alloy, *J. Am. Ceram. Soc.* 81 (1998) 1365–1368.
- [20] J. Tian, Z. Luo, S. Qi, X. Sun, Structure and antiwear behavior of micro-arc oxidized coatings on aluminum alloy, *Surf. Coat. Technol.* 154 (2002) 1–7.
- [21] A.G. Rakoch, V.V. Khokhlov, V.A. Bautin, N.A. Lebedeva, Y.V. Magurova, I. V. Bardin, Model concepts on the mechanism of microarc oxidation of metal materials and the control over this process, *Prot. Met.* 42 (2006) 158–169, <https://doi.org/10.1134/S003317320602010X>.
- [22] L. Zhu, Z. Guo, Y. Zhang, Z. Li, M. Sui, A mechanism for the growth of a plasma electrolytic oxide coating on Al, *Electrochim. Acta* 208 (2016) 296–303, <https://doi.org/10.1016/j.electacta.2016.04.186>.
- [23] G.A. Markov, V.I. Belevantsev, A.I. Slonova, O.P. Terleeva, Staging in anodic-cathodic microplasma processes, *Electrochemistry* 25 (1989) 1473–1479.
- [24] A. Nomine, J. Martin, G. Henrion, T. Belmonte, Effect of cathodic micro-discharges on oxide growth during plasma electrolytic oxidation (PEO), *Surf. Coat. Technol.* 269 (2015) 131–137, <https://doi.org/10.1016/j.surfcoat.2015.01.076>.
- [25] W. Gebarowski, S. Pietrzyk, Influence of the Cathodic Pulse on the Formation and Morphology of Oxide Coatings on Aluminium Produced by Plasma Electrolytic Oxidation, *Arch. Metall. Mater.* 58 (2013) 241–245, <https://doi.org/10.2478/v10172-012-0180-7>.
- [26] A.I. Slonova, O.P. Terleeva, Morphology, structure, and phase composition of microplasma coatings formed on Al-Cu-Mg alloy, *Prot. Met.* 44 (2008) 65–75, <https://doi.org/10.1134/S0033173208010098>.
- [27] A. Kramida, Y. Ralchenko, J. Reader, NIST ASD Team, NIST Atomic Spectra Database (ver. 5.5.6), [Online], (2018).
- [28] T.L. Burnett, Large volume serial section tomography by Xe Plasma FIB dual beam microscopy, *Ultramicroscopy* 161 (2016) 119–129.
- [29] P.W. Trimby, Orientation mapping of nanostructured materials using transmission Kikuchi diffraction in the scanning electron microscope, *Ultramicroscopy* 120 (2012) 16–24.
- [30] S. Suzuki, Features of Transmission EBSD and its Application, *JOM* 65 (2013) 1254–1264.
- [31] C.A. Schneider, W.S. Rasband, K.W. Eliceiri, NIH Image to ImageJ: 25 years of image analysis, *Nat. Methods* 9 (2012) 671–675.
- [32] A.B. Rogov, A. Nemcova, T. Hashimoto, A. Matthews, A. Yerokhin, Analysis of electrical response, gas evolution and coating morphology during transition to soft sparking PEO of Al, *Surf. Coat. Technol.* 442 (2022), 128142, <https://doi.org/10.1016/j.surfcoat.2022.128142>.
- [33] E.V. Parfenov, A. Yerokhin, A. Matthews, Small signal frequency response studies for plasma electrolytic oxidation, *Surf. Coat. Technol.* 203 (2009) 2896–2904, <https://doi.org/10.1016/j.surfcoat.2009.03.002>.
- [34] S. Tajima, Luminescence, breakdown and colouring of anodic oxide films on aluminium, *Electrochim. Acta* 22 (1977) 995–1011.
- [35] S. Stojadinovic, I. Belca, B. Kasalica, Lj. Zekovic, M. Tadic, The galvanoluminescence spectra of barrier oxide films on aluminum formed in inorganic electrolytes, *Electrochem. Commun.* 8 (2006) 1621–1624, <https://doi.org/10.1016/j.elecom.2006.07.035>.
- [36] J. Curran, T. Clyne, Porosity in plasma electrolytic oxide coatings, *Acta Mater.* 54 (2006) 1985–1993, <https://doi.org/10.1016/j.actamat.2005.12.029>.
- [37] J.G. Hooley, The kinetics of the reaction of silica with group I hydroxides, *Can. J. Chem.* 39 (1961) 1221–1230.
- [38] V.N. Malyshev, G.A. Markov, V.A. Fedorov, A.A. Petrosyants, O.P. Terleeva, Features of the structure and properties of coatings applied by the method of microarc oxidation, *Chem. Pet. Eng.* 20 (1984) 41–43.

- [39] V.A. Fedorov, Study of physical and mechanical characteristics and evaluation of wear resistance of the coatings, deposited by micro arc oxidation method, Proc. Gubkin's MINH&GP (1985) 22–39.
- [40] V.A. Fedorov, V.V. Belozero, N.D. Velikosek'skaya, S.I. Bulychev, Composition and structure of the reinforced surface layer on aluminium alloys, obtained under microarc oxidation, Phys. Chem. Mater. Treat. 4 (1988) 92–97.
- [41] V.A. Fedorov, N.D. Velikosek'skaya, Influence of microarc oxidation on the wear resistance of aluminium alloys, Friction and Wear 10 (1989) 521–524.
- [42] V.A. Fedorov, N.D. Velikosek'skaya, Relationship between the phase composition and properties of a hardened layer produced in microarc oxidation of aluminum alloys, Chem. Pet. Eng. 3 (1991) 29–30.
- [43] A.L. Yerokhin, A.A. Voevodin, V.V. Lyubimov, J. Zabinski, M. Donley, Plasma electrolytic fabrication of oxide ceramic surface layers for tribotechnical purposes on aluminium alloys, Surf. Coat. Technol. 110 (1998) 140–146, [https://doi.org/10.1016/S0257-8972\(98\)00694-X](https://doi.org/10.1016/S0257-8972(98)00694-X).
- [44] A. Yerokhin, A. Shatrov, V. Samsonov, P. Shashkov, A. Pilkington, A. Leyland, A. Matthews, Oxide ceramic coatings on aluminium alloys produced by a pulsed bipolar plasma electrolytic oxidation process, Surf. Coat. Technol. 199 (2005) 150–157, <https://doi.org/10.1016/j.surfcoat.2004.10.147>.
- [45] W. Xue, J. Du, X. Wu, Y. Lai, Tribological Behavior of Microarc Oxidation Coatings on Aluminum Alloy, ISIJ Int. 46 (2006) 287–291, <https://doi.org/10.2355/isijinternational.46.287>.
- [46] M. Sieber, T. Mehner, D. Dietrich, G. Alisch, D. Nickel, D. Meyer, J. Scharf, T. Lampke, Wear-resistant coatings on aluminium produced by plasma anodising—A correlation of wear properties, microstructure, phase composition and distribution, Surf. Coat. Technol. 240 (2014) 96–102, <https://doi.org/10.1016/j.surfcoat.2013.12.021>.
- [47] W. Xue, Z. Deng, R. Chen, T. Zhang, H.U.I. Ma, Microstructure and properties of ceramic coatings produced on 2024 aluminum alloy by microarc oxidation, J. Mater. Sci. 36 (2001) 2615–2619.
- [48] H.M. Nykyforchyn, M.D. Klapiv, V.M. Posuvailo, Properties of synthesised oxide-ceramic coatings in electrolyte plasma on aluminium alloys, Surf. Coat. Technol. 100–101 (1998) 219–221, [https://doi.org/10.1016/S0257-8972\(97\)00617-8](https://doi.org/10.1016/S0257-8972(97)00617-8).
- [49] L. Rama Krishna, K.R.C. Somaraju, G. Sundararajan, The tribological performance of ultra-hard ceramic composite coatings obtained through microarc oxidation, Surf. Coat. Technol. 163–164 (2003) 484–490, [https://doi.org/10.1016/S0257-8972\(02\)00646-1](https://doi.org/10.1016/S0257-8972(02)00646-1).
- [50] K. Tillous, T. Toll-Duchanoy, E. Bauer-Grosse, L. Hericher, G. Geandier, Microstructure and phase composition of microarc oxidation surface layers formed on aluminium and its alloys 2214-T6 and 7050-T74, Surf. Coat. Technol. 203 (2009) 2969–2973, <https://doi.org/10.1016/j.surfcoat.2009.03.021>.
- [51] A.B. Rogov, A. Yerokhin, A. Matthews, The role of cathodic current in plasma electrolytic oxidation of aluminium: current density 'scanning waves' on complex-shape substrates, J. Phys. D Appl. Phys. 51 (2018), 405303, <https://doi.org/10.1088/1361-6463/aad979>.
- [52] R.-S. Zhou, R.L. Snyder, Structures and Transformation Mechanisms of the eta, gamma, and theta Transition Alumina, Acta Crystallogr. B Struct. Crystallogr. Cryst. Chem. 47 (1991) 617–630.
- [53] T.W. Simpson, Q. Wen, N. Yu, D.R. Clarke, Kinetics of the Amorphous $\gamma \rightarrow \alpha$ Transformations in Aluminum Oxide: Effect of Crystallographic Orientation, J. Am. Ceram. Soc. 81 (1998) 61–66, <https://doi.org/10.1111/j.1151-2916.1998.tb02296.x>.
- [54] F. Balima, A. Largeteau, Phase transformation of alumina induced by high pressure spark plasma sintering (HP-SPS), Scr. Mater. 158 (2019) 20–23, <https://doi.org/10.1016/j.scriptamat.2018.08.016>.
- [55] I. Issa, L. Joly-Pottuz, J. Réthoré, C. Esnouf, T. Douillard, V. Garnier, J. Chevalier, S. Le Floch, D. Machon, K. Masenelli-Varlot, Room temperature plasticity and phase transformation of nanometer-sized transition alumina nanoparticles under pressure, Acta Mater. 150 (2018) 308–316, <https://doi.org/10.1016/j.actamat.2018.03.023>.
- [56] L.E. Fratila-Apachitei, F.D. Tichelaar, G.E. Thompson, H. Terryn, P. Skeldon, J. Duszczyk, L. Katgerman, A transmission electron microscopy study of hard anodic oxide layers on AlSi(Cu) alloys, Electrochim. Acta 49 (2004) 3169–3177, <https://doi.org/10.1016/j.electacta.2004.02.030>.
- [57] L. Campanella, A. Conte, A Comparison Between the Properties of Anodic Oxide Films on Aluminum Obtained in Different Alkali Nitrate Melts at Various Temperatures, J. Electrochem. Soc. 116 (1969) 144, <https://doi.org/10.1149/1.2411735>.
- [58] A. Sobolev, A. Kossenko, M. Zinigrad, K. Borodianskiy, An Investigation of Oxide Coating Synthesized on an Aluminum Alloy by Plasma Electrolytic Oxidation in Molten Salt, Appl. Sci. 7 (2017) 1–9, <https://doi.org/10.3390/app7090889>.
- [59] A. Sobolev, A. Kossenko, M. Zinigrad, K. Borodianskiy, Comparison of plasma electrolytic oxidation coatings on Al alloy created in aqueous solution and molten salt electrolytes, Surf. Coat. Technol. 344 (2018) 590–595.
- [60] M. Curioni, E.V. Koroleva, P. Skeldon, G.E. Thompson, Flow modulated ionic migration during porous oxide growth on aluminium, Electrochim. Acta 55 (2010) 7044–7049, <https://doi.org/10.1016/j.electacta.2010.06.088>.
- [61] A. Yerokhin, E.V. Parfenov, A. Matthews, In situ impedance spectroscopy of the plasma electrolytic oxidation process for deposition of Ca- and P-containing coatings on Ti, Surf. Coat. Technol. 301 (2016) 54–62, <https://doi.org/10.1016/j.surfcoat.2016.02.035>.
- [62] J.E. Houser, K.R. Hebert, The role of viscous flow of oxide in the growth of self-ordered porous anodic alumina films, Nat. Mater. 8 (2009) 415–420, <https://doi.org/10.1038/nmat2423>.
- [63] P. Chowdhury, A.N. Thomas, M. Sharma, H.C. Barshilia, An approach for in situ measurement of anode temperature during the growth of self-ordered nanoporous anodic alumina thin films: Influence of Joule heating on pore microstructure, Electrochim. Acta 115 (2014) 657–664, <https://doi.org/10.1016/j.electacta.2013.10.178>.
- [64] M. Schneider, C. Lämmel, C. Heubner, A. Michaelis, In situ temperature measurement on the metal/oxide/electrolyte interface during the anodizing of aluminium, Mater. Corros. 64 (2013) 60–68, <https://doi.org/10.1002/maco.201106129>.
- [65] C. Lämmel, M. Schneider, C. Heubner, W. Beckert, A. Michaelis, Investigations of burning phenomena during the hard anodising of aluminium by local in-operando temperature measurements, Electrochim. Acta 249 (2017) 271–277, <https://doi.org/10.1016/j.electacta.2017.07.167>.
- [66] R. McPherson, Formation of metastable phases in flame-and plasma-prepared alumina, J. Mater. Sci. 8 (1973) 851–858.
- [67] A.H. Tavakoli, P.S. Maram, S.J. Widgeon, J. Rufner, K. Benthem, S. Ushakov, S. Sen, A. Navrotsky, Amorphous alumina nanoparticles: Structure, Surface energy, and Thermodynamic phase stability, J. Phys. Chem. C 117 (2013) 17123–17130.
- [68] J.M. McHale, Surface Energies and Thermodynamic Phase Stability in Nanocrystalline Aluminas, Science 277 (1997) 788–791, <https://doi.org/10.1126/science.277.5327.788>.
- [69] M. Sieber, F. Simchen, R. Morgenstern, I. Scharf, T. Lampke, Plasma electrolytic oxidation of high-strength aluminium alloys - substrate effect on wear and corrosion performance, Metals 356 (2018) 1–17.
- [70] A.E. Gulec, Y. Gencer, M. Tarakci, The characterization of oxide based ceramic coating synthesized on Al-Si binary alloys by microarc oxidation, Surf. Coat. Technol. 269 (2015) 100–107, <https://doi.org/10.1016/j.surfcoat.2014.12.031>.
- [71] Y.-J. Oh, J.-I. Mun, J.-H. Kim, Effects of alloying elements on microstructure and protective properties of Al₂O₃ coatings formed on aluminum alloy substrates by plasma electrolysis, Surf. Coat. Technol. 204 (2009) 141–148, <https://doi.org/10.1016/j.surfcoat.2009.07.002>.
- [72] M. Tarakci, Plasma electrolytic oxidation coating of synthetic Al–Mg binary alloys, Mater. Charact. 62 (2011) 1214–1221, <https://doi.org/10.1016/j.matchar.2011.10.010>.
- [73] Z.C. Oter, Y. Gencer, M. Tarakci, The characterization of the coating formed by Microarc oxidation on binary Al–Mn alloys, J. Alloys Compd. 650 (2015) 185–192, <https://doi.org/10.1016/j.jallcom.2015.06.080>.
- [74] Y. Gencer, M. Tarakci, A.E. Gulec, Z. Cagay Oter, Plasma Electrolytic Oxidation of Binary Al–Sn Alloys, Acta Phys. Pol. A 125 (2014) 659–663, <https://doi.org/10.12693/APhysPolA.125.659>.
- [75] L. Zhu, W. Zhang, T. Zhang, J. Qiu, J. Cao, F. Wang, Effect of the Cu Content on the Microstructure and Corrosion Behavior of PEO Coatings on Al–x Cu Alloys, J. Electrochem. Soc. 165 (2018) C469–C483, <https://doi.org/10.1149/2.0471809jes>.
- [76] C.J.-P. Steiner, D.P.H. Hasselman, R.M. Spriggs, Kinetics of the Gamma-to-Alpha Alumina Phase Transformation, J. Am. Ceram. Soc. 54 (1971) 412–413, <https://doi.org/10.1111/j.1151-2916.1971.tb12335.x>.
- [77] K. Okada, A. Hattori, T. Taniguchi, A. Nukui, R.N. Das, Effect of Divalent Cation Additives on the γ -Al₂O₃-to- α -Al₂O₃ Phase Transition, J. Am. Ceram. Soc. 83 (2004) 928–932, <https://doi.org/10.1111/j.1151-2916.2000.tb01296.x>.
- [78] M. Ozawa, Y. Nishio, Thermal stability and microstructure of catalytic alumina composite support with lanthanum species, Appl. Surf. Sci. 380 (2016) 288–293, <https://doi.org/10.1016/j.apsusc.2015.12.246>.
- [79] M. Ozawa, M. Kimura, Effect of cerium addition on the thermal stability of gamma alumina support, J. Mater. Sci. Lett. 9 (1990) 291–293, <https://doi.org/10.1007/BF00725828>.
- [80] P. Burtin, J.P. Brunelle, M. Pijolat, M. Soustelle, Influence of surface area and additives on the thermal stability of transition alumina catalyst supports. II: Kinetic model and interpretation, Appl. Catal. 34 (1987) 239–254, [https://doi.org/10.1016/S0166-9834\(00\)82459-8](https://doi.org/10.1016/S0166-9834(00)82459-8).
- [81] L.A. Xue, I.-W. Chen, Influence of additives on the γ -to- α transformation of alumina, J. Mater. Sci. Lett. 11 (1992) 443–445.
- [82] Y. Saito, T. Takei, S. Hayashi, A. Yasumori, K. Okada, Effects of Amorphous and Crystalline SiO₂ Additives on γ -Al₂O₃-to- α -Al₂O₃ Phase Transitions, J. Am. Ceram. Soc. 81 (2005) 2197–2200, <https://doi.org/10.1111/j.1151-2916.1998.tb02608.x>.
- [83] A. Odaka, T. Yamaguchi, T. Fujita, S. Taruta, K. Kitajima, Cation dopant effect on phase transformation and microstructural evolution in M₂+substituted γ -alumina powders, J. Mater. Sci. 43 (2008) 2713–2720, <https://doi.org/10.1007/s10853-008-2485-5>.
- [84] C. Zeng, Y. Ling, Y. Bai, W. Liu, Y. Chen, Coupling effect of chromia doping and vacuum on the phase transition of alumina prepared by co-precipitation process, Powder Technol. 294 (2016) 284–291, <https://doi.org/10.1016/j.powtec.2016.02.045>.
- [85] R.H.R. Castro, D. Gouvêa, Efeito do íon Mn como aditivo na transição de fase $\gamma \rightarrow \alpha$ da alumina (Study of the influence of the Mn ion on the $\gamma \rightarrow \alpha$ alumina phase transition), Ceramica 49 (2003) 55–60.
- [86] G.C. Bye, G.T. Simpkin, Influence of Cr and Fe on Formation of alpha-Al₂O₃ from gamma-Al₂O₃, J. Am. Ceram. Soc. 57 (1974) 367–371, <https://doi.org/10.1111/j.1151-2916.1974.tb10925.x>.
- [87] G. Urretavizcaya, A.L. Cavalieri, J.M. Porto Lopez, I. Sobrados, J. Sanz, Thermal Evolution of Alumina Prepared by the Sol-gel technique, J. Mater. Synth. Process. 6 (1998) 1–7.
- [88] A.D. Polli, F.F. Lange, C.G. Levi, J. Mayer, Crystallization Behavior and Microstructure Evolution of (Al,Fe)O₃ Synthesized from Liquid Precursors, J. Am.

- Ceram. Soc. 79 (1996) 1745–1755, <https://doi.org/10.1111/j.1151-2916.1996.tb07991.x>.
- [89] A.R. Fatkullin, E.V. Parfenov, A. Yerokhin, D.M. Lazarev, A. Matthews, Effect of positive and negative pulse voltages on surface properties and equivalent circuit of the plasma electrolytic oxidation process, Surf. Coat. Technol. 284 (2015) 427–437, <https://doi.org/10.1016/j.surfcoat.2015.07.075>.
- [90] F.W. Dynys, J.W. Halloran, Alpha Alumina Formation in Alum-Derived Gamma Alumina, J. Am. Ceram. Soc. 65 (1982) 442–448, <https://doi.org/10.1111/j.1151-2916.1982.tb10511.x>.